

RESEARCH ARTICLE

10.1002/2016JD026373

Key Points:

- Hail precipitation rate is sensitive to initial environmental moisture change
- Hail precipitation rate responds to the initial water vapor profile nonlinearly in the second episode, while the total precipitation rate increases monotonically with initial moisture content
- Cold pool limits the hail production by limiting the development of deep convection and super cooled liquid water favors the hail production

Correspondence to:

Q. Zhang,
qzhang@pku.edu.cn

Citation:

Li, M., F. Zhang, Q. Zhang, J. Y. Harrington, and M. R. Kumjian (2017), Nonlinear response of hail precipitation rate to environmental moisture content: A real case modeling study of an episodic midlatitude severe convective event, *J. Geophys. Res. Atmos.*, 122, doi:10.1002/2016JD026373.

Received 13 DEC 2016

Accepted 8 JUN 2017

Accepted article online 11 JUN 2017

Nonlinear response of hail precipitation rate to environmental moisture content: A real case modeling study of an episodic midlatitude severe convective event

Mingxin Li^{1,2}, Fuqing Zhang² , Qinghong Zhang¹ , Jerry Y. Harrington², and Matthew R. Kumjian²

¹Department of Atmospheric and Oceanic Sciences, School of Physics, Peking University, Beijing, China, ²Department of Meteorology and Atmospheric Science, and Center for Advanced Data Assimilation and Predictability Techniques, Pennsylvania State University, University Park, Pennsylvania, USA

Abstract The dependence of hail production on initial moisture content in a simulated midlatitude episodic convective event occurred in northeast China on 10–11 June 2005 was investigated using the Weather Research and Forecasting (WRF) model with a double-moment microphysics scheme where both graupel and hail are considered. Three sensitivity experiments were performed by modifying the initial water vapor mixing ratio profile to 90% (“Q–10%”), 105% (“Q+5%”), and 110% (“Q+10%”) of the initial conditions used for the control simulation. It was found that increasing the initial water vapor content caused the hail and total precipitation rates to increase during the first 5 h. The precipitation response to increasing water vapor content was monotonic for this first episode; however, for the event’s second episode, the hail precipitation rate responds to the initial water vapor profile nonlinearly, while the total precipitation rate responds mostly monotonically. In particular, simulation Q+5% achieves the largest hail production rate while simulation Q+10% has the largest total precipitation rate. In contrast, during the second episode simulation Q–10% has the strongest vertical motion, produces the most cloud ice and snow, but has the lowest hail production. Analysis shows that increasing the initial moisture content directly increases the precipitation during the first episode, which subsequently induces a stronger, longer-lasting cold pool that limits the development of deep convection during the second episode.

1. Introduction

The ice phase plays an essential role in the development of the stratiform structure, precipitation, and longevity of mesoscale convective systems [Tao and Simpson, 1989; Tao et al., 1991, 1995; Chen and Cotton, 1988; Johnson et al., 1993, 1994; Yang and Houze, 1995; Braun and Houze, 1995, 1997]. Among the ice species, hail is of particular interest because of the damage it can cause [Cao, 2008; Carrió et al., 2014; Li et al., 2016] and its dynamic and thermodynamic impact on deep convection. For example, agricultural losses caused by hailstorms and other severe convection in China exceed the damage caused by tropical cyclones reaching 31.55 billion RMB in 2012 (CMA 2012). Hailstones, growing primarily by collecting supercooled cloud and raindrops, originate as millimeter-sized embryos (graupel or frozen drops) that are then transported into the main updraft region and continue to grow by collection of supercooled liquid water [e.g., Heymsfield et al., 1980; Heymsfield, 1982; Guo and Huang, 2002; Kennedy and Detwiler, 2003]. The final size of hailstones depends on supercooled liquid water concentration and the residence time of the hailstone in the updraft [e.g., Nelson, 1983; Ziegler et al., 1983; Rasmussen and Heymsfield, 1987]. Thus, an optimal hailstone growth environment requires appropriate storm-relative winds and updraft that can hold hailstones for a long time while not ejecting them into the anvil.

In turn, hail can influence storm precipitation and evolution through corresponding changes in dynamical and microphysical processes. Melting and sublimation of hail/graupel cool the air, which can lead to a stronger downdraft and colder outflow [e.g., Gilmore et al., 2004]. Using a hail growth model, Rasmussen and Heymsfield [1987] and Miller et al. [1988] found that the shedding of meltwater from hailstones results in substantial rainfall and droplet embryos in storms. Recycling of the shed meltwater may lead to more hail than would have been produced without shedding. Meanwhile, hail size can also impact storm structure: smaller hailstones are responsible for stronger low-level downdrafts, deeper and more intense cold pools, and greater low-level vertical vorticity in simulated supercells [van den Heever and Cotton, 2004].

Many prior studies have focused on the dependence of storm initiation, updraft intensity, and rainfall accumulation on moisture supply. For example, *Schlesinger* [1973] showed that greater moisture supply and weaker shear lead to more intense but short-lived convection. Moisture impacts on storm initiation have also been investigated. *Crook* [1996] found that convective initiation is sensitive to both surface temperature dropoff (the difference between the surface measured potential temperature and the boundary layer value) and moisture dropoff (the difference between the mixing ratio measured at the surface and the value in the lowest levels of the boundary layer), while the strength of well-developed convection is more sensitive to observed variability in moisture than temperature. In *Holloway and Neelin* [2009], higher column water vapor (mainly through entrainment) results in progressively greater plume buoyancies, indicating conditions favorable for deep convection. Based on the observational data from International H₂O Project [*Weckwerth et al.*, 2004], *Fabry* [2006] studied the importance of moisture variability on convection initiation, showing that the location of convection initiation is most sensitive to the temperature variability at synoptic scales and at the upper end of the mesoscale. While at smaller scales, although moisture variability is important, storm initiation was found to be more sensitive to convergence-driven updraft strength. *Schumacher* [2015] found that surface rainfall accumulation is reduced by a much larger fraction than the fraction by which the low-level moisture is reduced. The reason is that convection is less intense with drier subcloud layers because less air originating in that layer rises in convective updrafts.

Most recently, *Li et al.* [2016] showed that hail generation in northern China can be greatly impacted by reduced moisture availability due to the weakening of moisture transport by the weakened low-level meridional circulation after the 1990s. This research indicates a potential mechanism for moisture impacts on hail production and the resultant effects on deep convection: these can be understood in light of strong dependence of hail growth on ambient supercooled liquid water and storm intensity. However, only a few studies have been done on hail production in deep convection with regard to the ambient moisture supply. *Carrió et al.* [2014] investigated the cloud condensation nuclei (CCN) impact on hail with different amounts of low-level water vapor. They found that the CCN impact is weaker with higher low-level water vapor contents, as increasing CCN concentration led to a smaller enhancement in supercooled liquid water when warm rain processes were favored (i.e., in environments with greater low-level moisture content). *Grant and van den Heever* [2014] found that the presence of elevated dry layers led to different hail growth regions in simulated supercells: increased environmental dryness caused low-precipitation supercell structures with narrower and more tilted updrafts that together favored a downshear distribution of hydrometeors and hence favored hail fallout in the forward flank precipitation region. These studies mostly used an idealized model configuration initialized with a single thermodynamic profile and horizontally homogeneous environment. However, idealized numerical simulations show that convective storms can be influenced by environmental heterogeneities [e.g., *Richardson et al.*, 2007]. Thus, a real data simulation can more realistically represent these environmental heterogeneities that are likely present in the real atmosphere.

The current study investigates the nonlinear response of hail production to initial environmental moisture content, using an observed storm case. One control experiment and three sensitivity experiments using different initial environmental moisture profiles are performed using the WRF model. A description of the numerical model, the model setup, and the sensitivity experiments design are presented in section 2. The main results are presented in section 3. Summary and discussion are given in section 4.

2. Model Description and Experimental Design

The Advanced Research WRF [*Skamarock et al.*, 2008] version 3.7.1 is used for this study. The convective storm event that we simulate initiates around 1200 UTC 10 June 2005 over northeast China and dissipates after moving southeast over the Sea of Japan on 1200 UTC 11 June 2005. Large amounts of hail are produced during this severe event. The domain configuration is shown in Figure 1. The simulation uses three two-way-nested domains with 9 km, 3 km, and 1 km grid lengths, respectively. The outer domain (d01) covers most of north and northeast China with 433×394 grid points. Domain 2 (d02) has 655×526 grid points, and the inner domain (d03) has 982×868 grid points. We used 27 vertical levels which have seven levels below 1 km, and the grid is stretched to the model top at 50 hPa. The simulations were conducted with the Yonsei University (YSU) boundary layer scheme [*Hong et al.*, 2006], Noah Land Surface Model, Rapid Radiative Transfer Model longwave radiation scheme, and Dudhia shortwave radiation scheme. The Kain-Fritsch

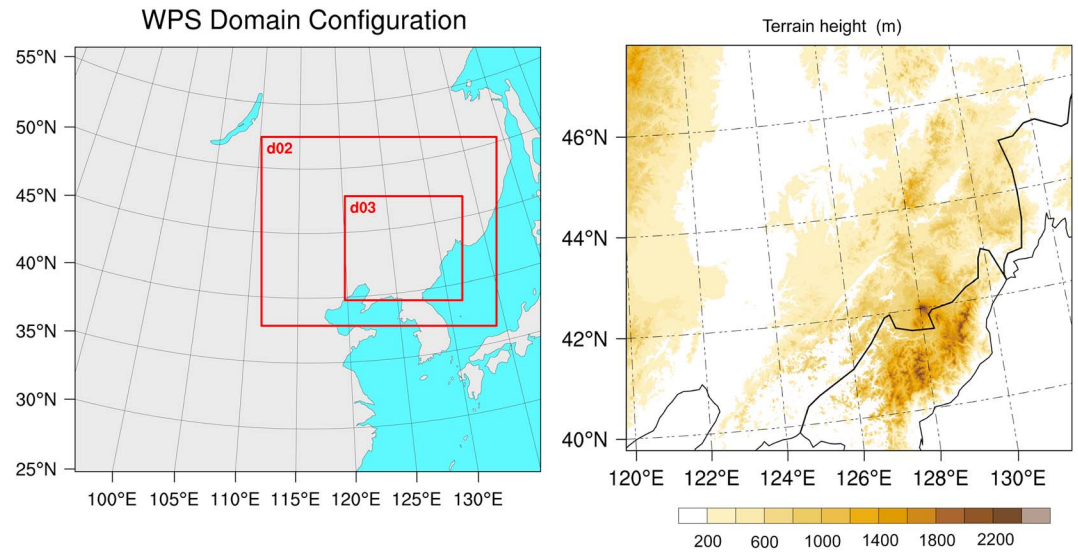


Figure 1. (left) Model domain configuration and (right) terrain height of d03 (shaded in meters MSL according to scale).

cumulus parameterization scheme is used for the d01 (no cumulus parameterization is used for d02 and d03). The bulk microphysics scheme employed here is the Milbrandt-Yau double-moment scheme (MY2) [Milbrandt and Yau, 2005a, 2005b], which predicts mass mixing ratio and number concentration for all seven hydrometeor categories (cloud, rain, ice, snow, graupel, and hail). After WRF version 3.6, the MY2 scheme has been updated to address several biases, including conversion processes from ice to snow and

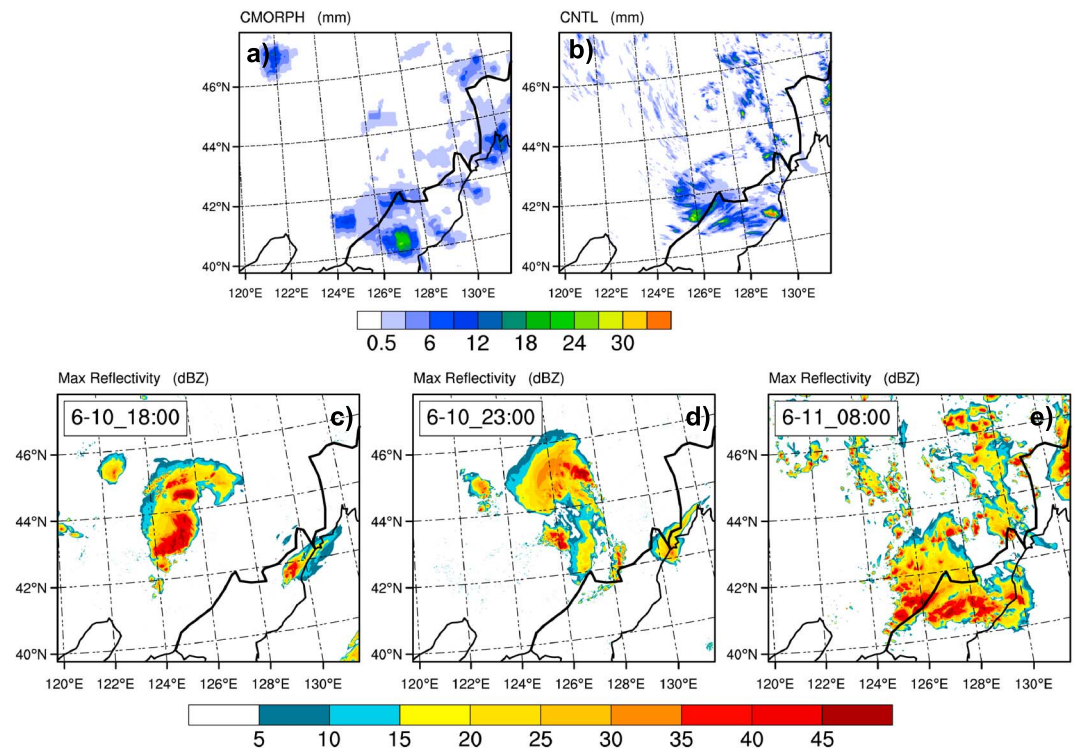


Figure 2. Total precipitation accumulation (in mm, shaded according to scale) during the most intense 2 h (0600–0800 UTC 11 June) from the (a) CMORPH data and (b) CNTL, and the general storm evolution (c) first episode, (d) dissipation, and (e) second episode of CNTL as seen through simulated column-maximum radar reflectivity at d03 (dBZ, shaded according to scale).

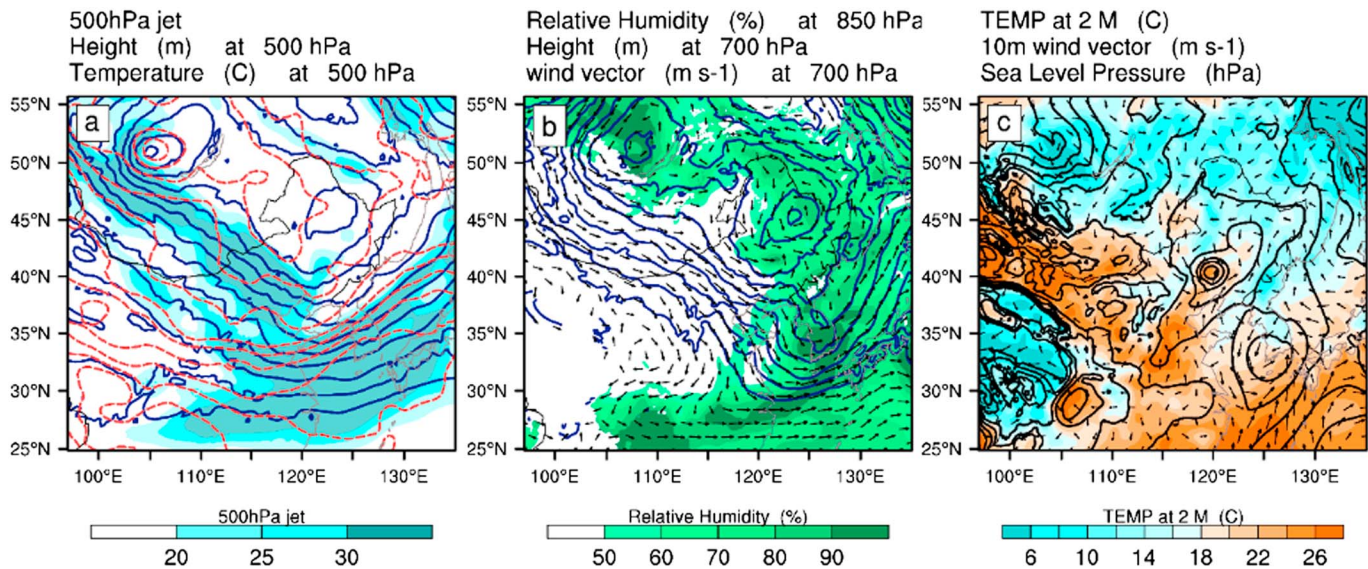


Figure 3. (a) Geopotential height (blue contour every 25 m from 5500 m to 5825 m), temperature (red dashed contour every 2°C from -22°C to -2°C) and winds (m s^{-1} , color shading) at 500 hPa; (b) relative humidity at 850 hPa (%), geopotential height (blue contour every 15 m from 2900 m to 3065 m) and horizontal wind (m s^{-1} ; black arrows) at 700 hPa; (c) temperature at 2 m ($^{\circ}\text{C}$, color shading), horizontal wind (m s^{-1}) at 10 m (black arrows) and sea level pressure (black contour every 2 hPa from 994 hPa to 1010 hPa). All panels are plotted at initial time (1200 UTC 10 June 2005) for d01.

from graupel to hail, which improve stratiform rain regions and overall reflectivity structure for an idealized squall line case [Morrison *et al.*, 2015]. The National Centers for Environmental Prediction Final (FNL) $1^{\circ} \times 1^{\circ}$ Operational Global Analysis data available every 6 h are used to generate the initial and lateral boundary conditions. The simulations are performed 30 h, from 1200 UTC 10 June 2005 to 1800 UTC 11 June 2005, covering the whole event from initiation through dissipation.

The purpose of these experiments is to capture the main characteristics of the event in order to investigate the sensitivity of hail production to changes in initial environmental moisture. As shown in Figure 2, despite the precipitation maximum and the northeast shifted rainfall location in control simulation (CNTL), the precipitation accumulation of the control simulation (CNTL) during the most intense 2 h (0600–0800 UTC 11 June) generally agrees with that derived from CMORPH (NOAA Climate Prediction Center Morphing Technique) precipitation data, suggesting that the CNTL simulation generally reproduces the evolution of the event. We also perform three sensitivity experiments designed to investigate whether and how initial moisture can influence the mesoscale convective storm and ultimately effect hail production. This is achieved by setting the model initial water vapor mixing ratio profile to 90%, 105%, and 110% of the CNTL simulation, respectively. Hereafter, these are referred to as Q–10%, Q+5%, and Q+10%, respectively. The rest of the model configurations are the same as in CNTL.

3. Simulation Results

3.1. General Description of Control Simulation

3.1.1. Synoptic Environment

Figure 3 shows the synoptic environment at the initial time of the simulation (1200 UTC 10 June 2005), before the storm initiates. At 500 hPa, a strong trough stretches from 100°E to 125°E longitude, to the north of China (Figure 3a), with two embedded geopotential height minima (550 dm and 555 dm, respectively). While the western low coincides with a temperature minimum, the eastern one is phase leading the isotherms, indicating ongoing intensification. Meanwhile, the -16°C isotherm covers a large area and stretches south to a latitude of 41°N , implying cold dry air at midlevels. Similar to 500 hPa, 700 hPa geopotential heights also show two embedded lows located at 110°E and 127°E longitude, respectively (Figure 3b). The convergence reflected by the southwesterly and southeasterly wind around 44°N and 123°E result in a local relative humidity (RH) maximum, which is where the storm eventually initiates. Much of the region is covered by a surface low-pressure system (Figure 3c). Southeasterly flow from the southeast side of the low-pressure system

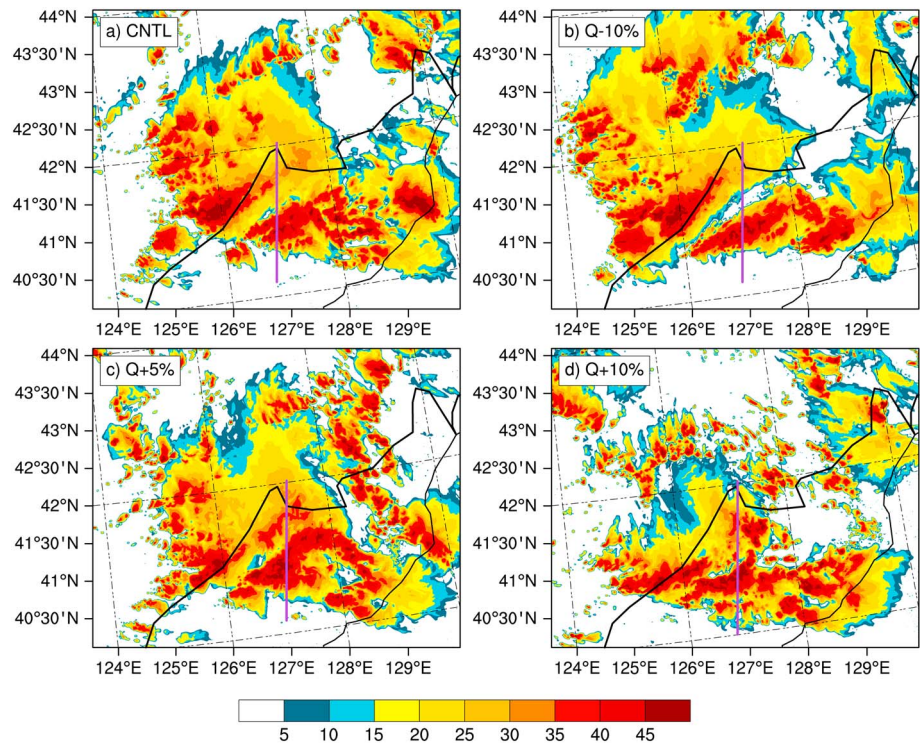


Figure 4. Simulated column-maximum radar reflectivity (dBZ, shaded according to scale) at the time of the hail precipitation rate maximum for each case. Purple lines show the location of the cross sections in Figure 11 and pass through location of maximum hail precipitation rate.

brings moisture from Bohai China Sea to the north (Figure 3c). The local RH maximum is just covered by both the 500 hPa jet and the 500 hPa thermal trough, which together provide the instability and shear for convective formation and development. The strong, steady 500 hPa low remains in place for at least the next 24 h, providing a favorable environment for a sequence of deep convective storms over northeast China.

3.1.2. CNTL Storm Evolution

As shown in Figures 2c–2e, there were two episodes of severe convection in this event being simulated. The initial episode began when storms initiated over the plains area and gradually developed into a linear convective system after 4 h of model initialization (1600 UTC 10 June; Figure 2c). The squall line persisted for several hours, during which large amounts of precipitation were produced. As the system moved eastward, this first episode of convection dissipated (Figure 2d). The storms associated with the second episode initiated at about 6–11_1:00 west of the mountains (indicated by darker shading in Figure 1, right). The storms quickly intensified and organized into a convective line that moved southward while approaching the mountains. At the same time, some isolated convective cells initiated on the southeast side of the mountain, fueled by the moistened air transported from the southeast. After several hours of development, the system in the north merged with the isolated convective cells and achieved its maximal intensity (Figure 2e). During this period, the largest hail precipitation accumulation occurred on the mountains, which is our focus in this work.

3.2. Topography Effects

During the first episode, storms mainly occurred over the plains area and dissipated before reaching the mountainous region; therefore, topography plays little role in this first episode. However, during the second episode, new convective cells initiate to the northwest of the mountains and develop as they approach the mountain. Figure 4 shows the simulated column-maximum radar reflectivity (hereafter “radar reflectivity”) at the time of the maximum hail precipitation rate (0940 UTC 11 June for Q–10%, 0800 UTC for CNTL and Q+5%, and 0740 UTC for Q+10%) for the four simulations. The storm intensity maximizes over the mountains. Recall that the original linear convective system merged with the isolated convective cells on the mountain and

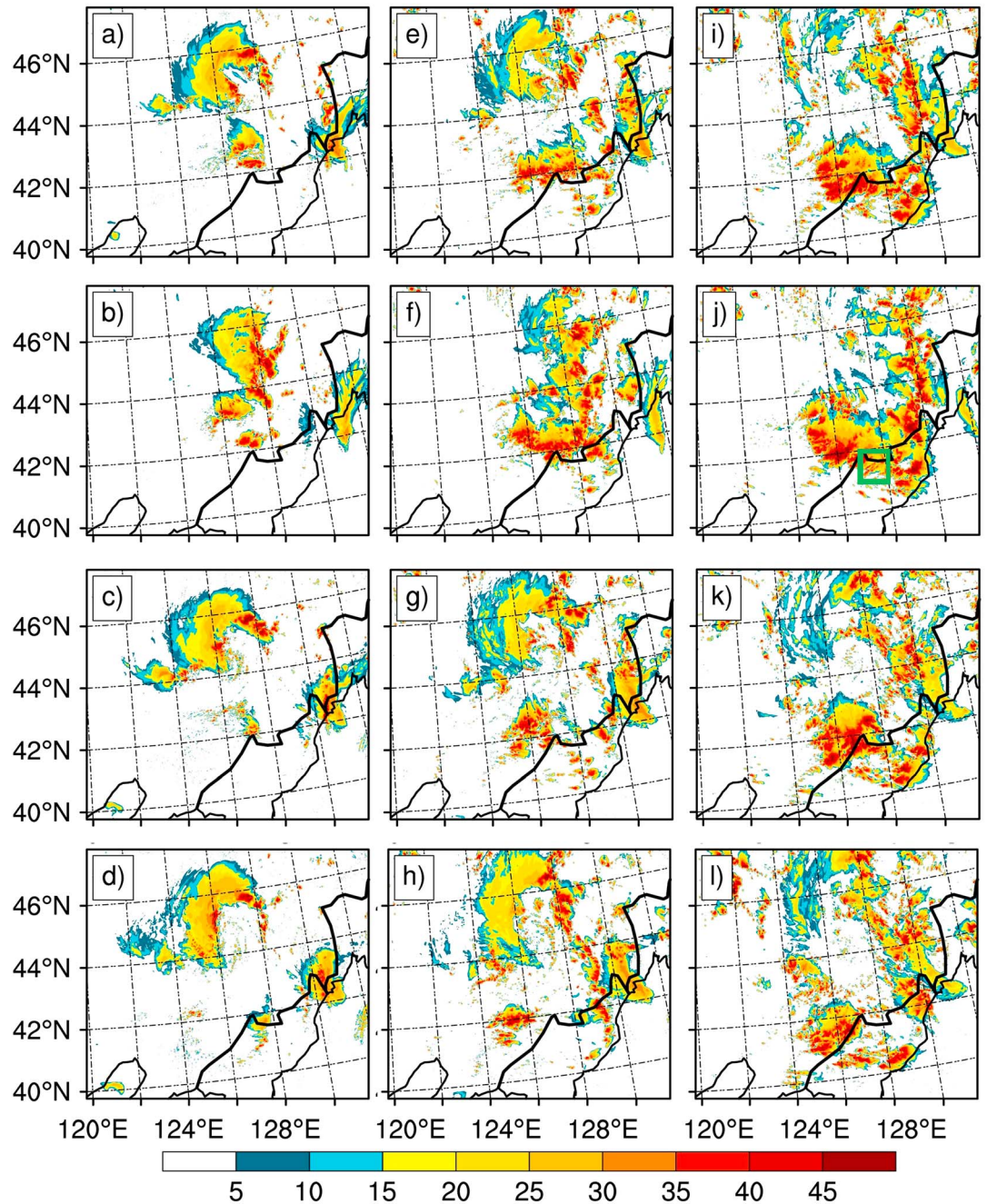


Figure 5. Simulated column-maximum radar reflectivity (dBZ, shaded according to scale) for (a, e, and i) CNTL, (b, f, and j) Q−10%, (c, g, and k) Q+5%, and (d, h, and l) Q+10% at 0200 UTC 11 June (Figures 5a–5d), (Figures 5e–5h) 0400 UTC 11 June, and (Figures 5i–5l) 0600 UTC 11 June for d03.

subsequently intensified. Additionally, topographic lifting enhanced storm intensity. Further, because of lower temperatures at the higher elevations, more hail can reach the ground before melting. The fact that the maximum hail precipitation rate occurred on the mountain for all four simulations stresses the significance of topographic effects for hail production in this case.

3.3. Storm Evolution of Sensitivity Simulations

Figure 5 shows the storm evolution in the four experiments represented by the radar reflectivity. At 0200 UTC 11 June, right after conclusion of the first episode for all experiments (convection located around 44–46°N

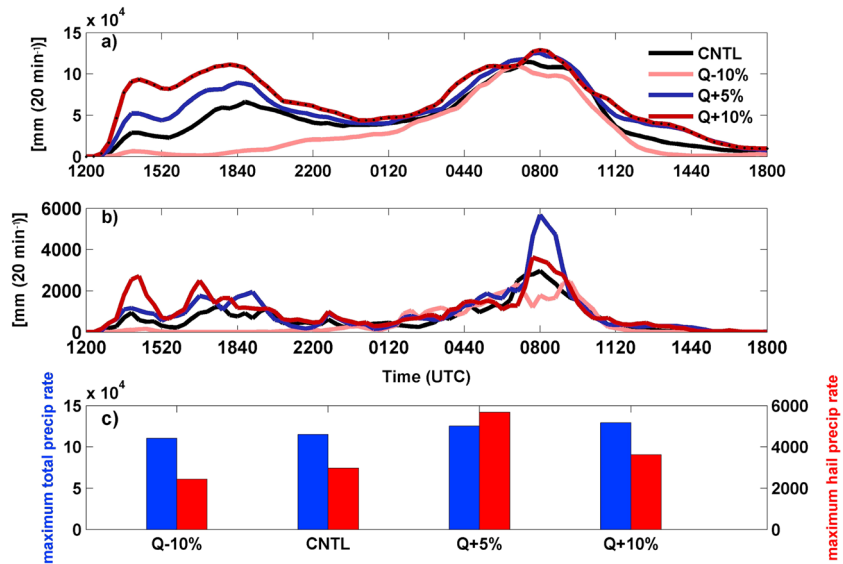


Figure 6. Domain-integrated 20 min mean (a) precipitation rate and (b) hail precipitation rate, and (c) the maximum domain-integrated precipitation rate (blue bar) and hail precipitation rate (red bar) for CNTL and sensitivity experiments. Unit is (mm (20 min⁻¹)) for all panels.

and 124°E–128°E dissipated), new convective activities of the second episode (located around 127°E–42°N) begin to emerge (Figures 5a–5d). After two more hours, differences are apparent among the four simulations. As shown in Figures 5e–5h, convection in Q–10% is well organized into a coherent (squall) line over a large area between 42°N–43°N and 125°E–129°E. CNTL has also developed into a squall line but much weaker than Q–10%. In contrast, corresponding convective activities in Q+5% and Q+10% are still scattered. At 0600 UTC 11 June (Figures 5i–5l), the convective activities in Q–10% are further intensified with convective cells moving up to the mountains to the east. Convection in Q+10% is the weakest (and westmost) among all simulations.

Storm evolution can be represented by the domain total (all the domain total or domain average are calculated through d03 hereafter if unspecified) 20 min mean precipitation rate throughout the event (Figure 6a). Similar to CNTL, Q+5% and Q+10% also have two episodes during their storms’ lifetime. Q+10% develops a little earlier than Q+5%, and they both grow sooner than CNTL because adding water vapor makes it easier for air parcels to reach saturation. In contrast, Q–10% does not initiate at all for the first 6 h. Instead, it is suppressed by the water vapor reduction and only begins to grow after 6 h into the simulation; as a result: the Q–10% event only has one episode of convection.

Despite the earlier convective initiation and evolution in the Q+5% and Q+10% sensitivity experiments, the difference in storm intensification is more obvious during the first convective episode. CNTL achieves its maximum precipitation rate during the first episode after 7 h, whereas Q+5% and Q+10% achieve their precipitation rate maxima 20 min earlier than CNTL. Notice Q+10% has twice the maximum precipitation rate of CNTL; the Q+5% maximum precipitation rate falls approximately in the middle of Q+10% and CNTL, indicating a monotonic relation between maximum of precipitation rate and initial moisture content for the first convective episode. Q–10% begins to develop from 1800 UTC 10 June and attains a much smaller precipitation rate for 6 h compared to the other simulations. After 12 h into the simulation, the first episode ends and the second episode commences. During the second episode, although the precipitation rate is larger in the experiments with more water vapor, the differences between cases are smaller.

The precipitation rate for only hail is shown in Figure 6b. Although there exist more fluctuations in hail precipitation rate than in the total precipitation rate, the overall tendency for the first episode is similar to what is observed for the total precipitation rate. For the second episode, the hail precipitation rate shows a markedly different trend from the total precipitation rate: the Q–10% hail precipitation rate exceeds the other experiments from 0200 to 0400 UTC 11 June and then reaches a maximum at about 0900 UTC. In contrast, the other

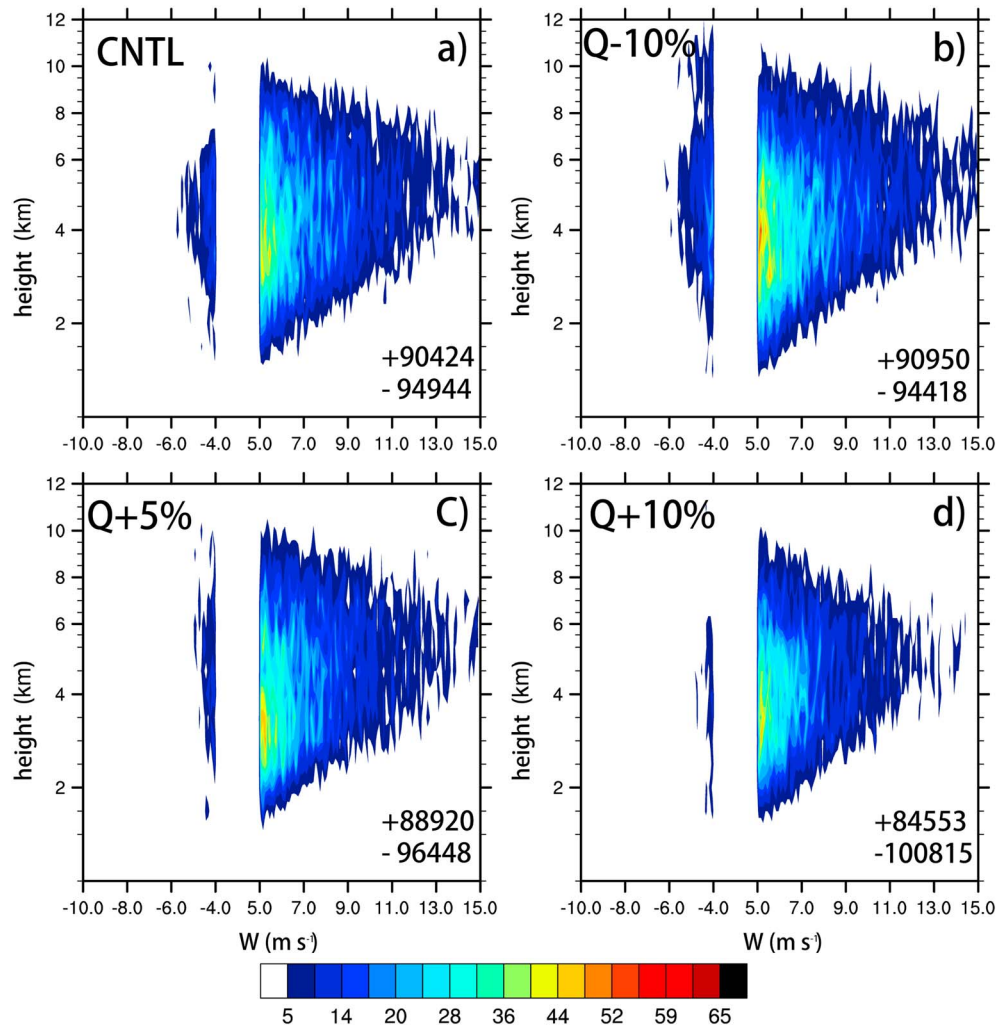


Figure 7. Frequency distributions of the vertical velocity (m s^{-1}) at 06-11_07:40 as a function of altitude for domain the same as in Figure 4 of all four simulations. Shading indicates count of grid points. Vertical velocity that are less than 5 m s^{-1} and larger than -4 m s^{-1} are not sampled here. Count of grid points of $w > 0$ (+) and $w < 0$ (-) at 6 km are shown at bottom right corner for each panel.

cases reach their maxima at about 0740 UTC. More importantly, the relation between hail precipitation rate and initial water vapor content is no longer monotonic: Q+5% exhibits the largest hail precipitation rate, followed by Q+10%, CNTL, and Q-10%. The maxima of the domain-integrated hail and precipitation rates from different simulations are shown in Figure 6c, which clearly illustrates a monotonic response of the maximum domain-integrated precipitation rate and a nonlinear response of the maximum domain-integrated hail precipitation rate to the initial water vapor content. The reasons for this nonlinear behavior will be discussed in a subsection below.

3.4. Dynamics

3.4.1. First Episode

The sensitivity experiments demonstrate that storm initiation occurs earlier (Figure 6) for cases with larger moisture content. Particularly at low levels, the enhanced moisture reduces stability and allows lifted parcels to more readily achieve saturation, lowering lifted condensation levels. This increases the likelihood that parcels reach their level of free convection and tap into the environmental conditional instability. The decreased moisture in the Q-10% case leads to increased stability. This increased stability prevents convective inhibition and does not initiates until about 6 h after the simulation begins.

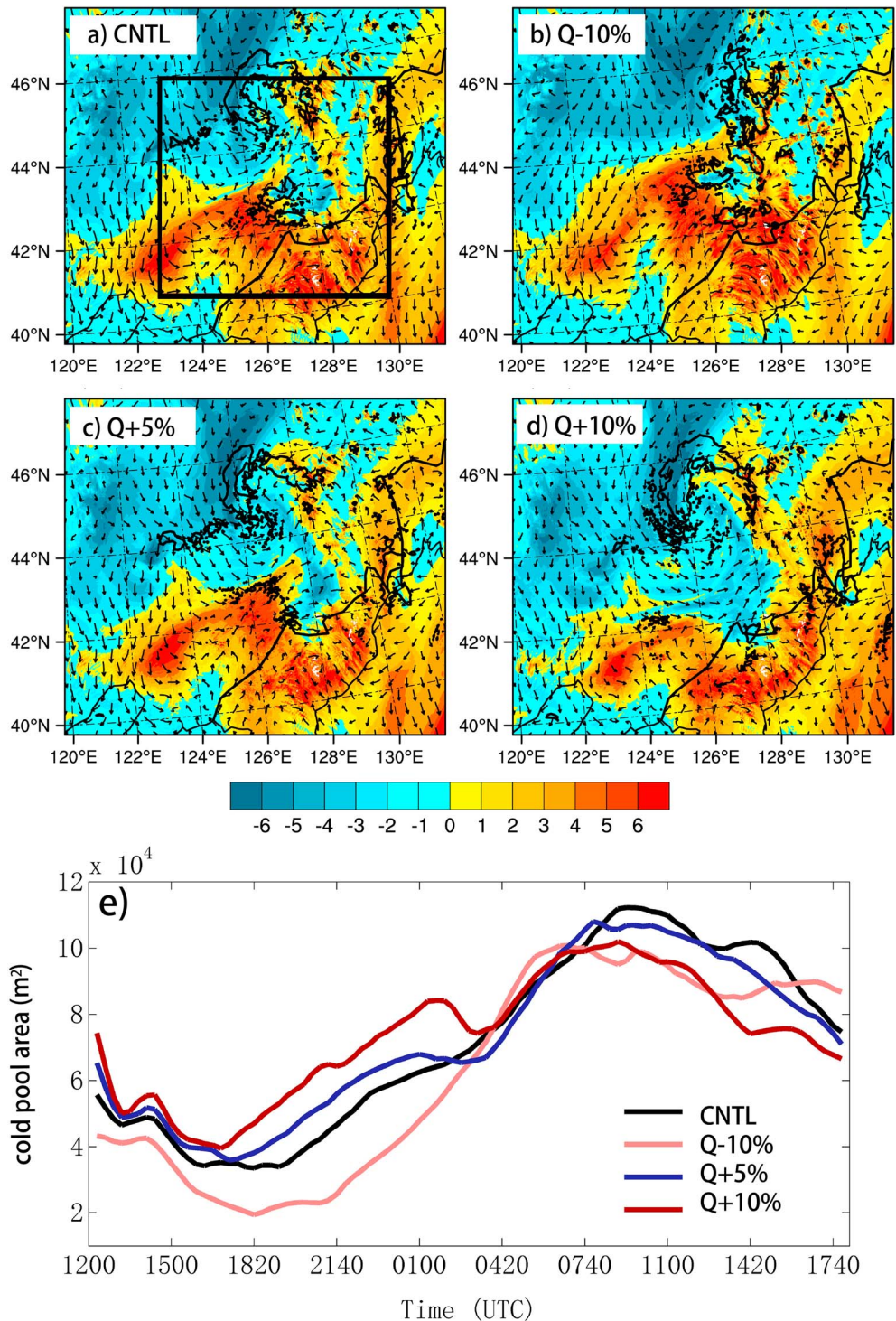


Figure 8. (a-d) θ_e perturbation at 0100 UTC 11 June (in K, shaded according to scale) for all experiments. Vectors represent wind at 10 m and black lines mark the 35 dBz radar reflectivity contours. (e) The time series of cold pool area (m²) only calculated for the area shown in the CNTL panel by black box.

After initiation, as indicated by hail and total precipitation rates (Figure 6), the simulations with increased water vapor lead to more intense convection that undergoes more rapid morphological changes (as seen from the radar reflectivity evolution of the first episode, not shown); Q+10% generates the most intense storm as measured by both precipitation rate and vertical motion (not shown). Additionally, increasing

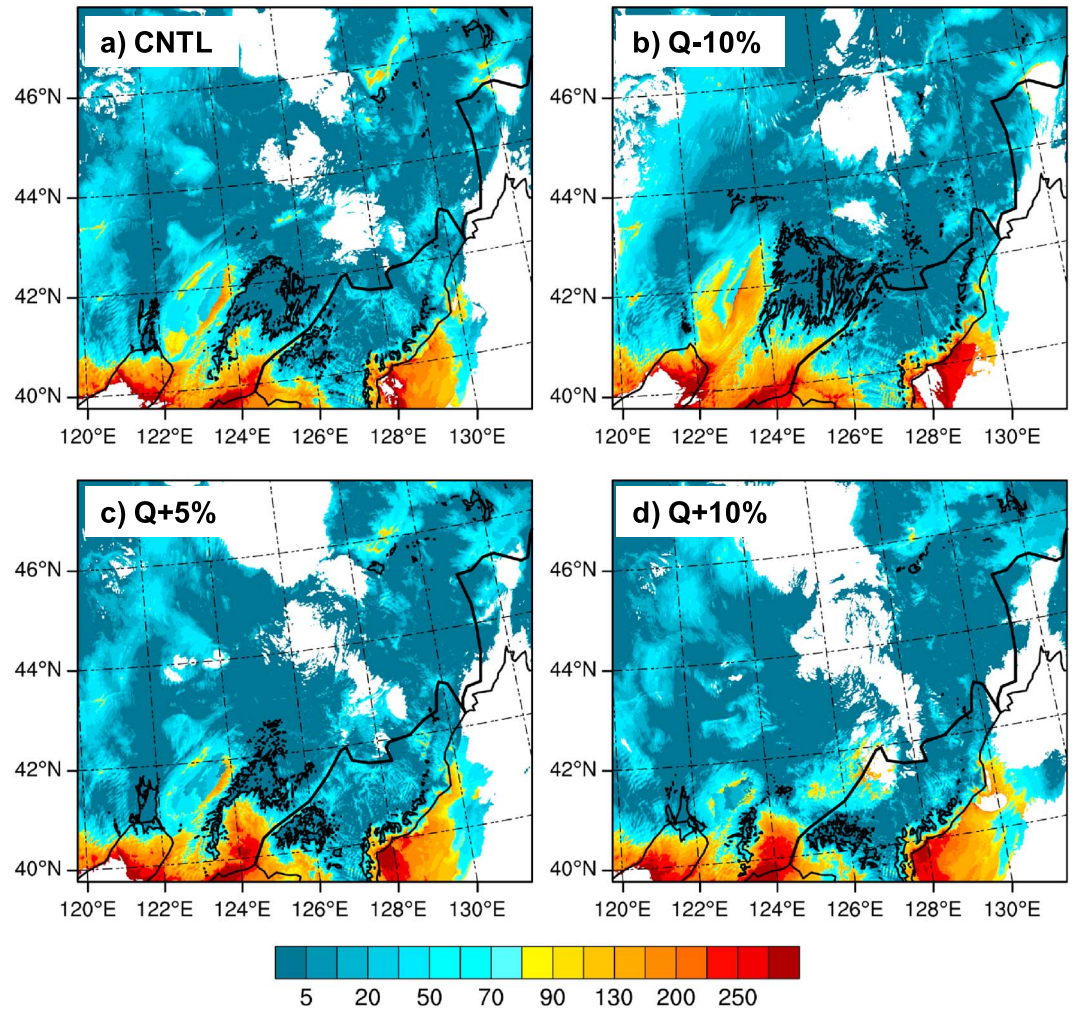


Figure 9. Maximum CIN ($J\ kg^{-1}$; shaded according to scale) and CAPE $> 1500\ J\ kg^{-1}$ (black lines) at the same time as Figures 8a–8d.

initial water vapor directly reduces environmental convection inhibition (CIN) and consequently enlarges the area over which air parcels can overcome CIN and achieve their level of free convection (LFC) given essentially the same initial lifting across all simulations (resulting from large-scale ascent and/or localized heterogeneities associated with low-level boundaries). As a result, storms initiate over a much wider area, which means that the Q+10% simulation has a larger region of convection and, subsequently, a larger region of precipitation (not shown). More widespread convection results in more condensational latent heating, which in turn intensifies the storm system itself.

To summarize, modifying the initial water vapor profile plays a direct role in the first episode. Both the total precipitation rate and hail precipitation rate increase with increasing initial moisture content. As a result of increased cloud and precipitation formation (latent heating), the convection is more intense and leads to greater amounts of precipitation. For this stage, hail production, which is related to storm intensity, is directly affected by changes to the initial water vapor profile.

3.4.2. Second Episode

The first convective episode is essentially finished 12 h into the simulation for CNTL, Q+5%, and Q+10%. (Recall that because of the relative dearth of moisture in Q–10%, a convective system did not develop until much later than the other experiments.) The second episode commences at 0100 UTC 11 June for all experiments. While Q+10% maintains the largest total precipitation rate for the remaining time, the Q + 5% hail

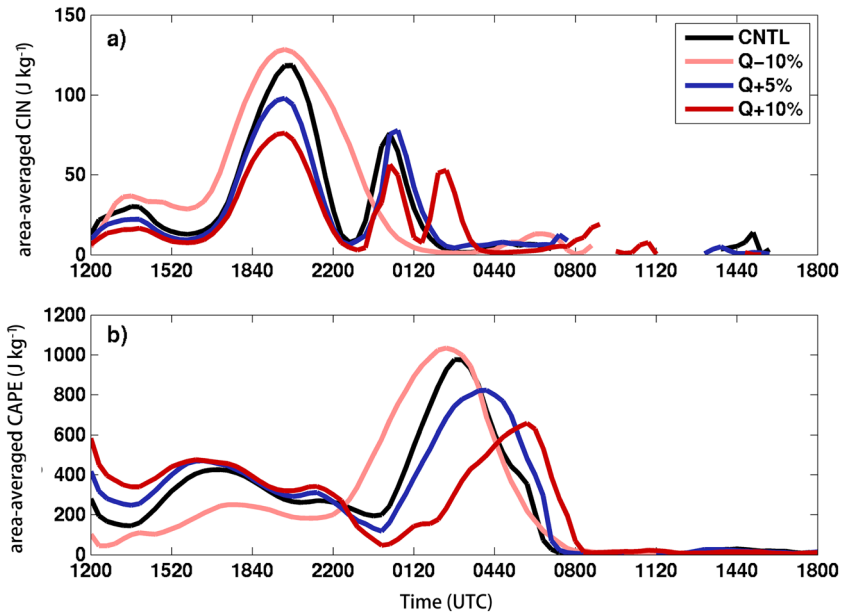


Figure 10. Box-averaged (a) CIN and (b) CAPE time series for all experiments. The box is shown in Figure 5j. If the parcel does not have LFC, CIN is treated as missing value in Figure 10a.

precipitation rate exceeds Q+10%, becoming the largest among all the experiments, indicating that *modifying the initial water vapor profiles ultimately has nonlinear impacts on hail precipitation rate.*

Radar reflectivity in Q+10% reveals more widely scattered convection in this episode rather than organized convection characteristic of the other experiments (Figure 4). Q-10% is in a quite intense state where the convective cells are most well organized. Though convective organization is similar in CNTL and Q+5%, the strongest convection in Q+5% is over the mountainous terrain, whereas CNTL has the stronger convection northwest of the high terrain. To quantify domain-wide convective intensity, we plot frequency distributions of vertical velocity for the same domain as in Figure 4 at 0740 UTC 11 June (Figure 7), when the system entered an intense state for all experiments (domain total precipitation maximizes around this time). Maximal vertical velocity is located at around 6 km above ground level for all experiments. Interestingly, both the magnitude of vertical motion and the spatial coverage of updraft and strong downdraft ($w < -4 \text{ m s}^{-1}$) in Q-10% are larger than the other three experiments. CNTL and Q+5% feature similar intensity, except that CNTL has slightly stronger downdrafts. Q+10% has the weakest vertical motion at this time. Count of grid points of updraft (+) and downdraft (-) at 6 km are shown at the bottom right corner for each panel. It can be seen that Q+10% has a wider but weaker downdraft than others.

Figure 8 shows the equivalent potential temperature perturbation (defined as difference between local θ_e and the domain average θ_e at the same level) at 2 km 0200 UTC 11 June. For CNTL, it is clear that storms to the north from the first episode have weakened and new cells have emerged on the south near 43°N and 127°E for Q+5% and Q+10%, new cells are just initiating along the airmass boundaries (i.e., boundaries between the positive and negative θ_e perturbations); for Q-10%, the convection is developing into a well-organized storm. A cold pool (defined as θ_e perturbation $< -2 \text{ K}$) mainly induced by evaporative cooling can be seen from the dark blue region along the positive area of θ_e perturbation (e.g., between 127°E-129°E and 42.5°N-44°N in Figure 8a). Based on the cold pool definition above, we can determine the total cold pool area for each simulation as a function of time (Figure 8e). For the period before 0200 UTC 11 June, Q+10% kept the most widespread cold pool, followed by Q+5%, CNTL, and Q-10%. Thus, at this stage, the cold pool area is dictated more by precipitation production than initial water vapor content. With larger initial moisture, first-episode storms were more intense and produced larger amounts of precipitation, leading to greater evaporative cooling and forming larger cold pool areas. These cold pools persisted and affected convective initiation and evolution in the second episode. To illustrate the cold pool effects, we calculate the convection inhibition (CIN) and convective available potential energy (CAPE) (Figure 9). At this time, Q-10% has the

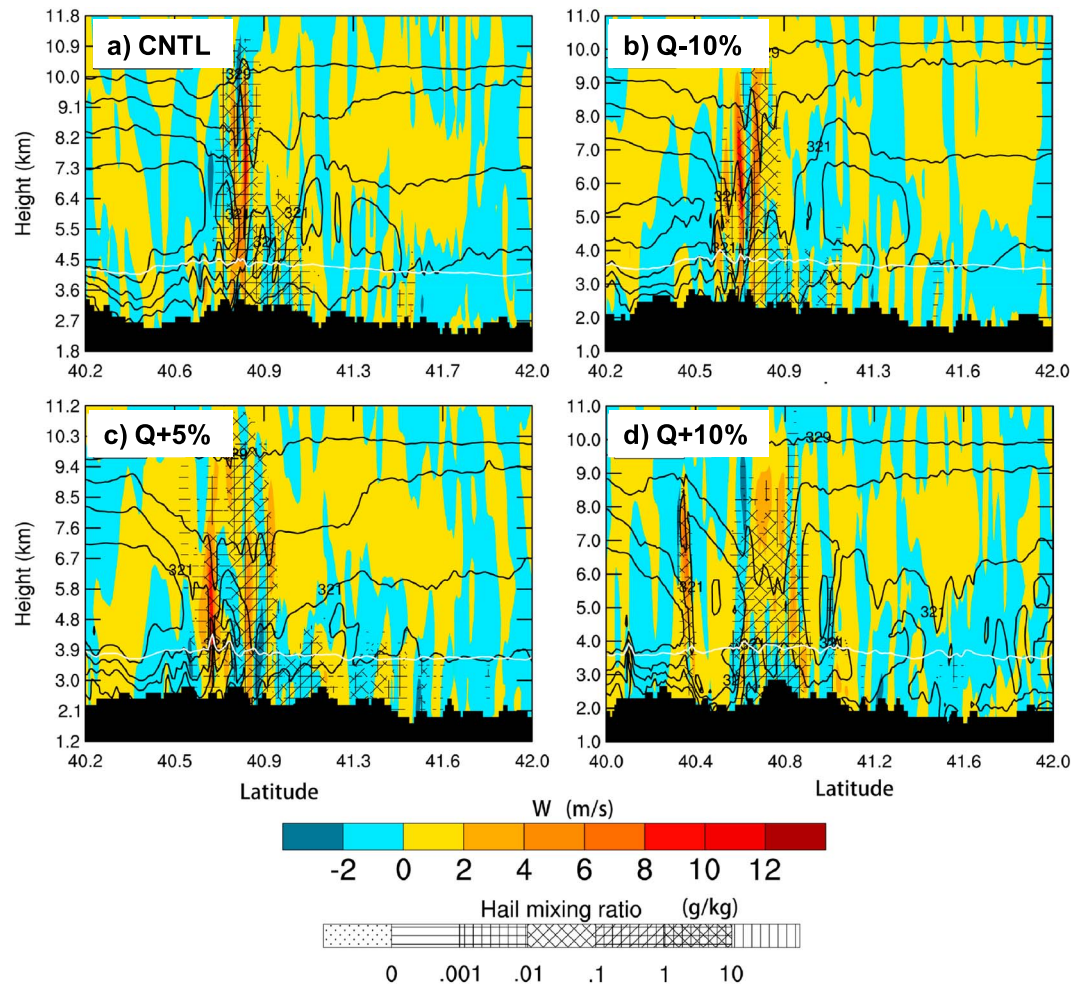


Figure 11. Cross sections as indicated in Figure 4. Hatching represents hail mass mixing ratio (g kg^{-1}). Color shading indicates vertical velocity (m s^{-1}) and black contours denote the equivalent potential temperature (K). White line indicates the melting level. Terrain is shown as black shading.

smallest CIN and larger CAPE (black contours circle the area where $\text{CAPE} > 1500 \text{ J kg}^{-1}$) among all simulations. In contrast, Q+10% has the largest CIN and least CAPE, which limits convective initiation and storm intensity. As a result, storm intensity of the second episode reverses order of the first episode. Q-10% becomes the most intense storm followed by CNTL, Q+5%, and Q+10%. Time series of box-averaged CIN and CAPE are also calculated and are shown in Figure 10. The box (shown with green box in Figure 5j) is chosen within the cold pool area where new convective cells in Q-10% pass through but the convective cells in Q+10% bypass. For Q-10%, CIN drops to the lowest while CAPE is the largest among all simulations during 0100–0400 UTC when the second episode initiates and develops. For this reason, convective activities in Q+10% are weaker and are limited much more to the west which fail to well unite with the convective cells originated on mountainous area. Consequently, Q+10% cannot develop a well-organized convective system.

Vertical cross sections through the region of maximum hail precipitation rate (Figure 11) show that the updraft is taller but narrower in CNTL and Q-10 compared to Q+5% and Q+10%, while regions of hail in Q+5% and Q+10% are wider than CNTL and Q-10%. This is reasonable because the updraft width is an important factor in hail growth [e.g., Nelson, 1983; Foote, 1984; Dennis and Kumjian, 2017]. However, hail mass mixing ratio in Q+10% does not reach as high in altitude as other simulations, a result of its weaker updrafts during this episode.

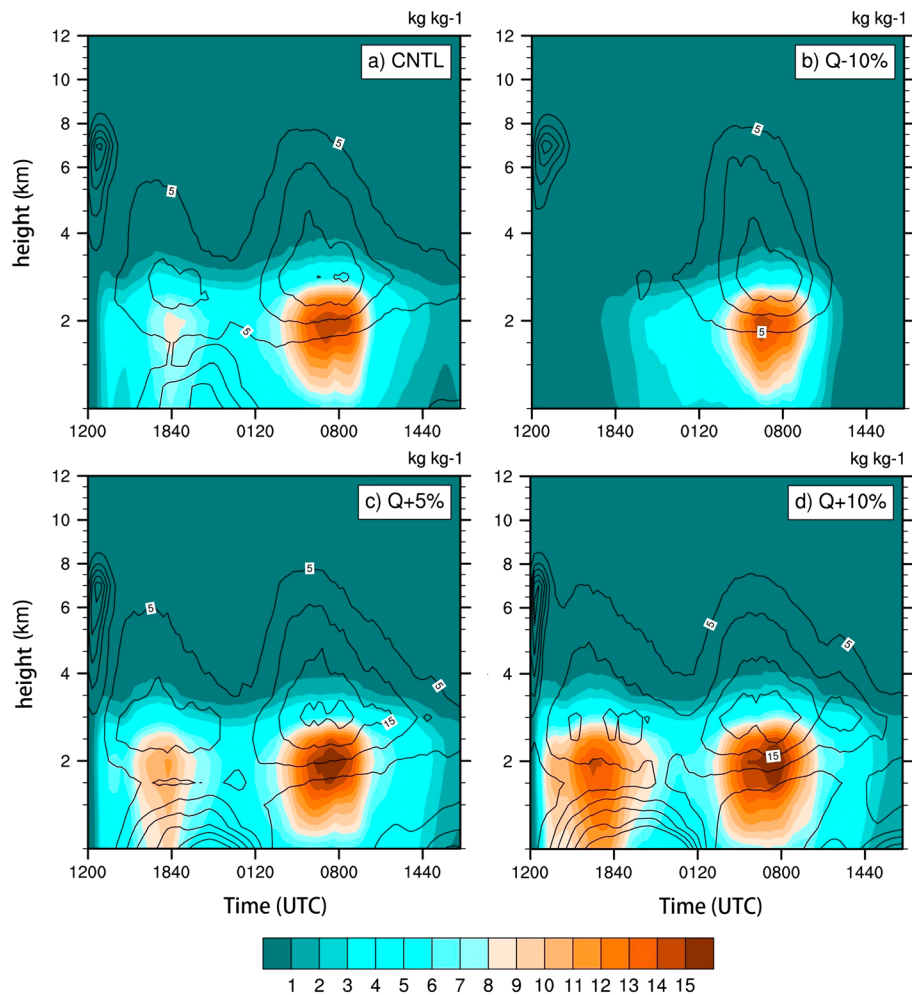


Figure 12. Domain total rain water mass mixing ratio (kg kg^{-1} , shaded according to scale) and cloud water mass mixing ratio (contoured from 5 to 30 every 5, unit is kg kg^{-1}) as a function of time and altitude for all experiments.

To summarize, convective storms during the second episode display a different (nonlinear) response to the initial moisture profiles than those during the first episode. Even though the total precipitation rate still displays a relatively monotonic relation with initial water vapor changes, hail precipitation rate shows nonlinear response such that Q+5% exhibits the largest hail precipitation rate. Moreover, hail precipitation rate cannot be completely interpreted by storm intensity; there may be microphysical effects affecting hail precipitation rates. These are discussed in the following subsection.

3.5. Microphysics

Figure 12 illustrates the domain total cloud water mass mixing ratio (black contour) and rain water mass mixing ratio (color shading) as a function of time and altitude for all four experiments. The cloud water mass mixing ratio experiences a jump in the first 2 h for all simulations. This rapid increase is associated with the model spin-up process. After that, large cloud water mixing ratio is mainly located below 1 km for CNTL, Q+5%, and Q+10% during the first episode, suggesting active warm rain processes are important for the first stage. During the second episode, patterns of cloud water distribution are similar between different simulations and mixing ratio maxima are located at 3 km. Unsurprisingly, Q+10% has the largest amount of cloud water throughout the entire simulation time. Characteristics of rain water mixing ratio is similar to that of cloud water: two episodes can be clearly seen, except for the absence of first episode in Q-10%. Rain water mixing ratio maxima are located at 2 km for all simulations. Thus, the liquid water contents are closely associated with initial water vapor in this case for all simulations.

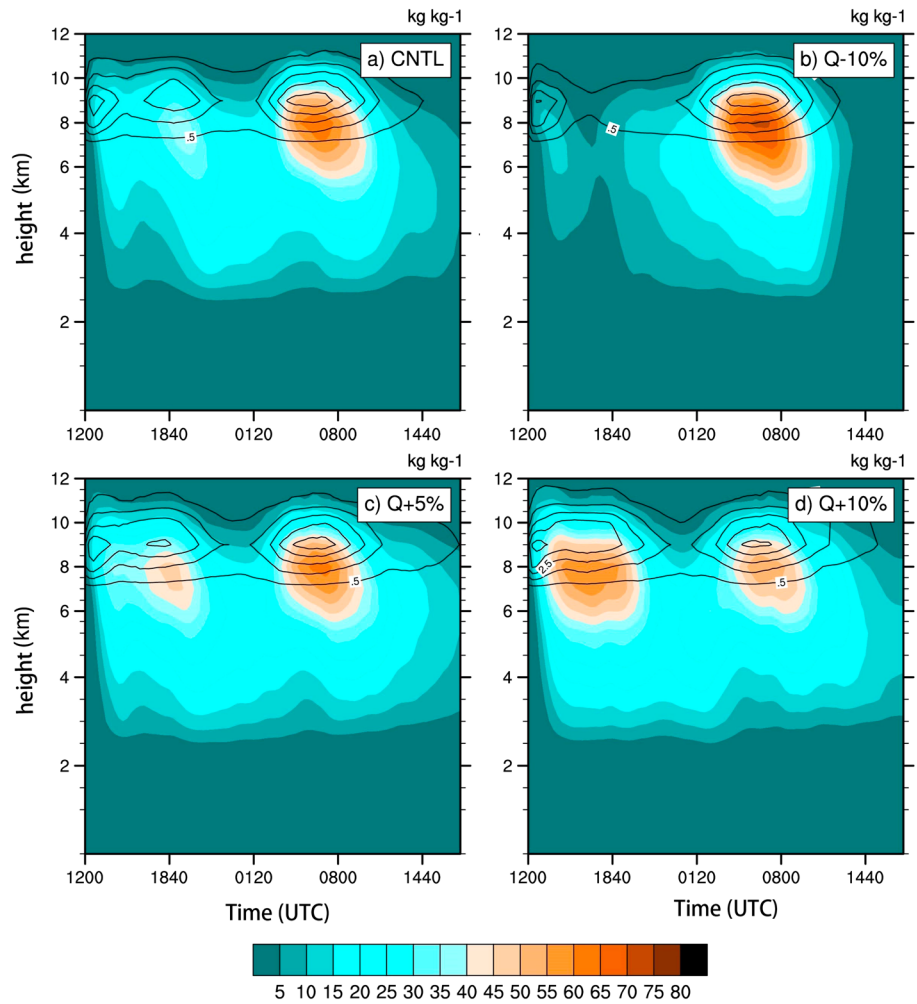


Figure 13. Same as Figure 12 but for domain total snow mass mixing ratio (kg kg^{-1} , shaded according to scale) and domain total ice mass mixing ratio (contoured from 0.5 to 5.5 every 1 kg kg^{-1}).

Cloud ice and snow are found to behave differently from liquid water. Cloud ice (black contour in Figure 13) is distributed above 8 km, with maxima near 9 km. Similar to cloud water, cloud ice also exhibits a jump in the first 2 h. The total cloud ice mass amount has a positive correlation with total cloud water mass during the first episode, meaning that experiments with more initial water vapor produce more cloud ice. Snow mass (color shading in Figure 13), which predominantly arises from aggregation of cloud ice, has a high correlation with ice mass and also shows a positive correlation with initial water vapor amount for the first episode. However, for the second episode, both ice and snow amount in Q+10% are less than the other experiments; instead, Q−10% produces the most cloud ice and snow. Being the most intense convective system during the second episode, Q−10% exhibits the strongest downdraft and largest vertical motion, which can bring more water vapor into upper troposphere for cloud ice formation and growth via vapor deposition. Subsequently, larger cloud ice mass leads to larger snow mass via aggregation. With the lowest CAPE (Figure 9), updrafts in Q+10% are the weakest (Figure 7); hence, Q+10% produces the least amount of cloud ice and snow. Differences in cloud ice and snow between CNTL and Q+5% similarly can be attributed to differences in vertical motion during the second episode.

As the rimed ice species (and thus dependent on both liquid and ice contents), graupel and hail show interesting behaviors that differ from the other hydrometeor species. Large graupel and hail mass regions are centered at 6 km and 3 km, respectively, for all simulations (Figure 14). Differences in graupel and hail mass in the first episode are similar to those observed in cloud ice and snow and exhibit a positive

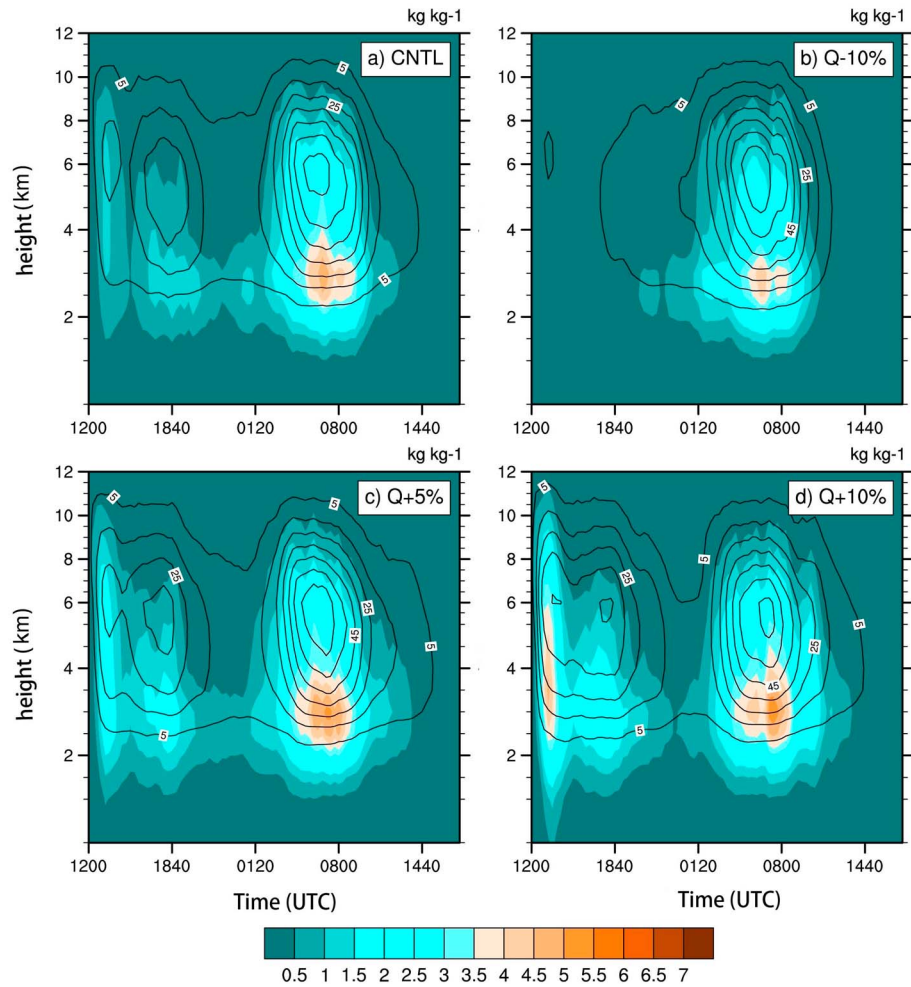


Figure 14. Same as Figure 12 but for domain total hail mass mixing ratio (kg kg^{-1} , shaded according to scale) and domain total graupel mass mixing ratio (contoured from 5–65 every 10 kg kg^{-1}).

correlation with initial water vapor profiles. For the second episode, however, Q–10% and Q+5% produce the most graupel mass, whereas Q+10% produces the least graupel mass. The major graupel source is snow that has undergone riming. Because of the large quantity of snow mass in Q–10%, it is expected to have large amount of graupel due to the conversion from snow via riming. However, a large amount of supercooled liquid water is also needed for riming. The Q+5% case produces large amounts of supercooled cloud water that compensates for the relatively reduced snow mass, producing considerable amounts of graupel. When the snow number concentration is roughly equal as it is between CNTL and Q+5%, the one with more supercooled liquid water (Q+5%) produces more graupel.

Focusing on hail production, we investigate the hail growth via collection of supercooled liquid cloud and rain water (Figure 15). Note that the collection rates account for both supercooled liquid water and hail mixing ratio. The Q+10% case shows the largest riming rates, suggesting that supercooled liquid water content dominates the riming rate; decreasing supercooled liquid water content (Q+10% > Q+5% > CNTL > Q–10%) decreases the combined hail riming rates. These microphysical effects play a significant role in hail production: Q+10% produces the most hail mass aloft, followed by Q+5%, CNTL, and Q–10%. In the MY2 scheme, graupel is also a major source for hail. When graupel grows to a considerable size via riming, it is converted to the hail category. In our experiments, Q–10% exhibits the most graupel mass during the second episode, which suggests that the conversion process should be larger than for the other simulations. However, upon inspection of the domain total snow and graupel number concentrations (Figure 16), which illustrate the conversion processes among snow, graupel, and hail, we see that graupel number

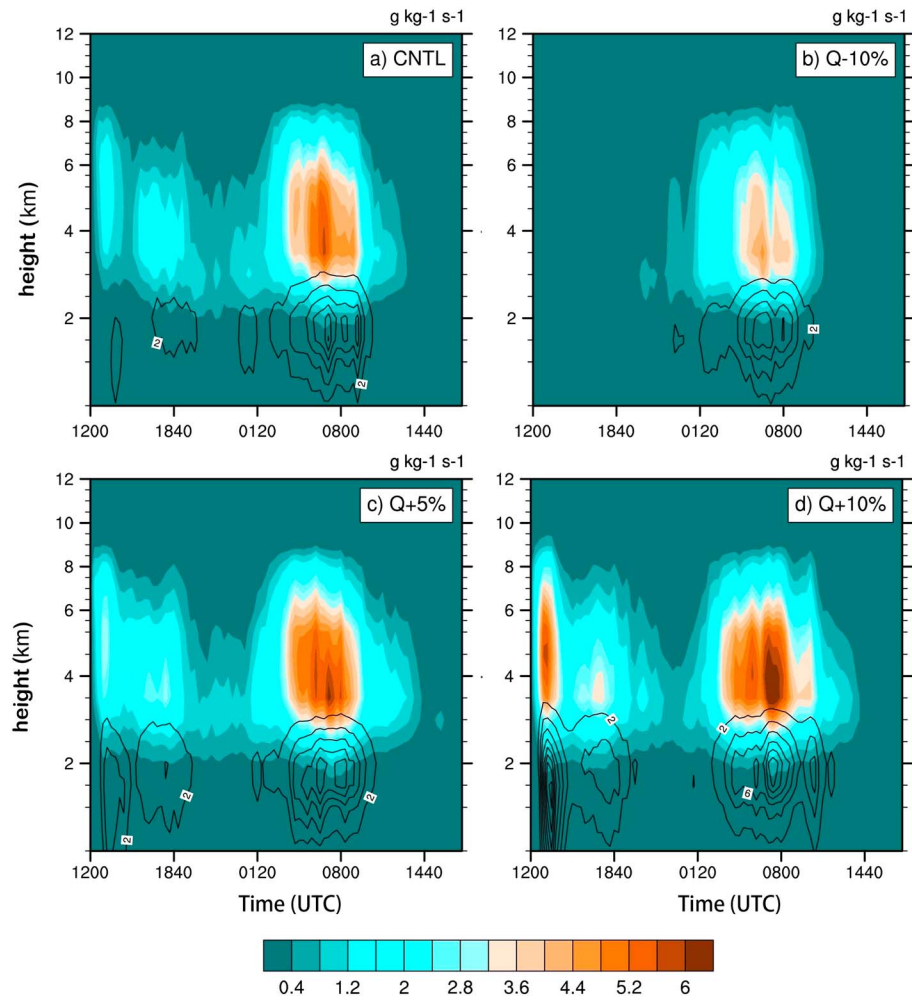


Figure 15. Same as Figure 12 but for rate of the process rate of hail collecting cloud water droplets ($\text{g kg}^{-1} \text{s}^{-1}$, shaded according to scale) and the microphysical process rate of hail collecting rain water (contoured from 2–16 every $2 \text{ g kg}^{-1} \text{s}^{-1}$).

concentration for Q–10% is large enough during the second episode such that there is competition for the supercooled liquid water, which is quite limited in this case. Hence, it is the supercooled liquid water content that limits graupel growth and subsequently sizes, keeping much of the graupel mass from converting to hail. This is why Q–10% exhibits the most graupel but least hail.

The large hail precipitation rate comes from the combined effects of storm structure, microphysical processes, and interaction with high topography. With large amounts of liquid water, Q+5% is capable of robust riming growth of hail. At the same time, it maintains a considerably large vertical motion and storm intensity in the second episode. When moving across the mountain area, Q+5% produces the largest amount of hail precipitation, which is at least in part due to less melting (the freezing level in Q+5% is lower than that in Q+10%, Figure 17) with higher terrains before the hail mass reaches the ground. Thus, despite a monotonic response in hail production aloft to initial water vapor concentrations, there is a nonlinear response in the *hail precipitation rate*.

4. Summary and Discussion

In this study, we conducted a series of sensitivity simulations for a midlatitude deep convective storm event initiated at 10 June 2006 in northeast China to investigate the effects of initial environmental moisture content on the storm structure and evolution. In particular, we focus on the response of hail production to small

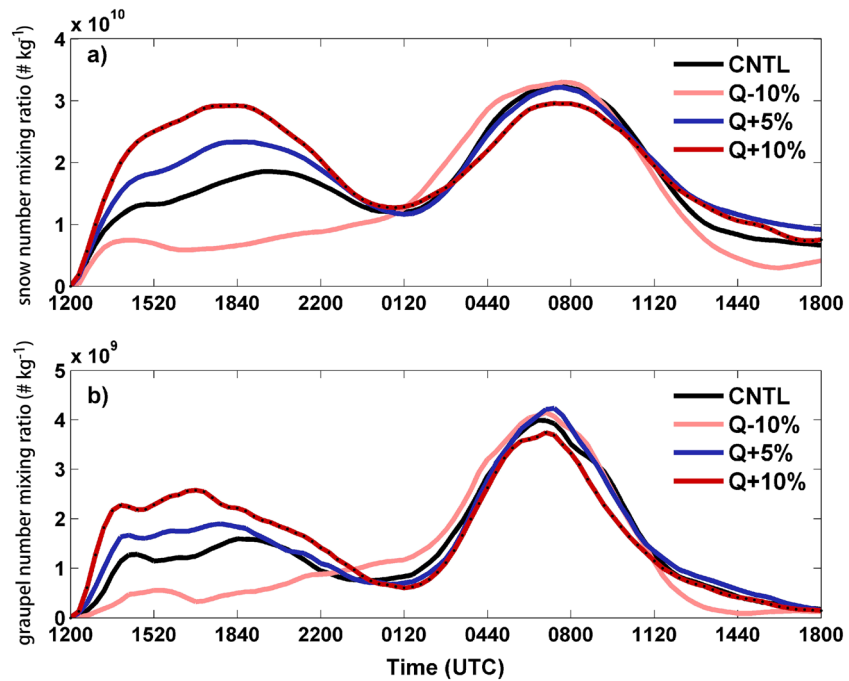


Figure 16. Domain total number mixing ratio ($\# \text{ kg}^{-1}$) of (a) snow and (b) graupel in cloud vary with time.

changes in the initial water vapor profiles. Overall, both the total precipitation rate and the hail precipitation rate are sensitive to initial moisture changes.

The event consisted of two main convective episodes. The first episode is directly influenced by the amount of initial water vapor, exhibiting a positive monotonic correlation between domain total precipitation rate/hail precipitation rate and initial water vapor content. The second episode, however, is more strongly affected by the residual cold pool produced during the first episode rather than the moisture changes in the initial environment. Experiments with different initial water vapor during the second episode still show monotonicity on domain total precipitation rate but the differences in storm intensity among the simulations have decreased compared to in the first episode. Domain total hail precipitation rate shows a significant nonlinear response that results from both dynamical (storm intensity) and microphysical effects (supercooled water supply) brought by the changes in initial moisture.

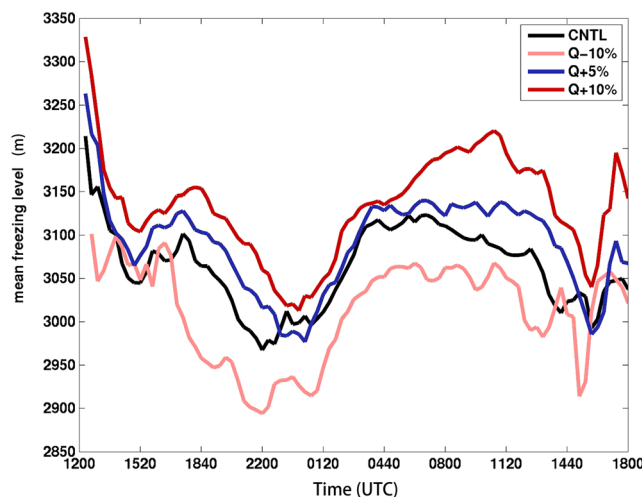


Figure 17. Mean freezing level (averaged within d03 where mdBZ > 35) time series.

Consistent with previous studies using idealized simulations [e.g., Schumacher, 2015], the storm system produces more total precipitation and displays a larger total precipitation rate when increasing initial moisture. Consequently, more widespread cold pools are generated by more the intense storms, which also produce greater rainfall. Previous studies have placed a great deal of emphasis on the cold pool's effects in initiating new convective cells and its contribution to storm maintenance and longevity, which are directly related to cold pool intensity. In this study, the influences are

mainly caused by the *spatial coverage* of the cold pool. In the second convective episode, new convective cells are just initiating in CNTL, Q+5%, and Q+10%, whereas Q−10% has already developed into a mature convective system with new cells initiating along its cold pool edges.

Simulations with more initial water vapor are expected to evaporate less than those with drier environmental conditions. Indeed, the moister simulations produce cold pools with weaker temperature deficits; however, these storms generally produce cold pools with greater area extent (Figure 8). Cooling from melting and sublimation of ice particles also contributes to cold pool generation [e.g., *Braun and Houze*, 1995], but the increased melting rates under moister conditions are not sufficient to overcome decreases in evaporation, the primary contribution to cooling.

The initial moisture differences affect the event evolution in notable ways. For example, CNTL, Q+5%, and Q+10% all feature two distinct convective episodes, whereas Q−10% begins much later (i.e., the first episode is largely absent). The absence of the first episode gives the prestorm environment in Q−10% the opportunity to slowly accumulate moisture needed for convection initiation. In contrast, storms in the second episode of the other simulations are suppressed by the large CIN and reduced CAPE associated with the leftover cold pool from the first episode. As a result, Q+10% has the weakest storm during the second episode. Thus, the nonlinear response of total hail precipitation rate can be partially attributed to the storm intensity differences in the second process.

Domain total hail precipitation rate is significantly influenced by microphysical processes in this case. There is more liquid water (cloud water and rain water) produced as the initial moisture increased. However, the cloud ice and snow mass are less in the second episode than when the initial condition is drier. This is due to the dynamical response of weaker vertical motion, as mentioned above. Stronger updrafts in Q−10% in the second episode make it possible to transport more water vapor to higher levels, which provides a rich source of water vapor for the formation and growth of cloud ice and snow. For the second episode, Q−10% and Q+5% contain the most graupel, while Q+10% produces the largest amount of hail aloft in spite of storm intensity. Large amounts of snow lead to more graupel in Q−10%, while the lack of supercooled liquid water limits the conversion to and growth of hail. In contrast, cases with more cloud water and rain water lead to larger hail riming rates. As a result, Q+10% produces the most hail mass, followed by Q+5%. Therefore, the effect of supercooled liquid water is more important than the vertical motion for total hail formation in clouds in this case. But hail on the ground still largely depend on dynamical structure of the storm and influence of the topography.

Under such a favorable synoptic pattern for convection in this case, there exists a large possibility that a sequence of convective storms are generated. Changes in thermodynamics from large areas of precipitation and intense cold pools also greatly impact subsequent convective cell initiation and intensity, which in turn impacts hail production. More importantly, increasing the moisture content in the environment directly impacts the microphysical processes active in the storm. More specifically, hail growth is largely modified by the changes in supercooled liquid water, which can be regarded as an indirect effect from the changes of initial moisture content profiles.

One caveat is that the microphysics scheme used herein is a double-moment bulk scheme in which there exists a graupel-hail conversion process. Even though we used the modified version of MY2 in which the portion of graupel that undergoes wet growth is converted to hail, it is still only a crude representation of hail processes in atmosphere. Growth of graupel and hail are both greatly influenced by supercooled liquid water content, which limits the diameters that hail or graupel can attain via riming. In the MY2 scheme, the integrated particle size distribution is treated in bulk and thus does not account for the nuances of different sized particles. As the rimed ice species in the scheme, hail and graupel are treated very similarly: the main difference between them is their prescribed fall speed and density [*Morrison and Milbrandt*, 2011; *Bryan and Morrison*, 2012]. It is inevitable that uncertainties associated with the conversion process exist in the bulk scheme, but a better representation of this process is out of the scope of this study.

References

- Braun, S. A., and R. A. Houze (1995), Melting and freezing in a mesoscale convective system, *Q. J. R. Meteorol. Soc.*, *121*, 55–77.
- Braun, S. A., and R. A. Houze (1997), The evolution of the 10–11 June 1985 PRE-STORM squall line: Initiation, development of rear inflow, and dissipation, *Mon. Weather Rev.*, *125*, 478–504.

Acknowledgments

Computing is conducted at the Texas Advanced Computing Center where the WRF model output is stored that can be made freely available upon request. This study is supported by the Chinese National Science Foundation under grants 41330421 and 41461164006. J. Harrington was supported by the U.S. Department of Energy's Atmospheric Science Program Atmospheric System Research, and Office of Science, Office of Biological and Environmental Research Program under grant DE-SC0012827. The first author conducted the research while a visiting scholar at the Pennsylvania State University. M.K. was partially supported by a grant from the Insurance Institute for Business and Home Safety. The first author thanks Yaosheng Chen and Bicheng Chen from Pennsylvania State University for helpful discussions and suggestions. The first and third authors gratefully acknowledge the financial support from the China Scholarship Council.

- Bryan, G. H., and H. Morrison (2012), Sensitivity of a simulated squall line to horizontal resolution and parameterization of microphysics, *Mon. Weather Rev.*, *140*, 202–225.
- Cao, Z. (2008), Severe hail frequency over Ontario, Canada: Recent trend and variability, *Geophys. Res. Lett.*, *35*, L14803, doi:10.1029/2008GL034888.
- Carrió, G. G., W. R. Cotton, and A. M. Loftus (2014), On the response of hailstorms to enhanced CCN concentrations, *Atmos. Res.*, *143*, 342–350.
- Chen, S., and W. R. Cotton (1988), The sensitivity of a simulated extratropical mesoscale convective system to longwave radiation and ice-phase microphysics, *J. Atmos. Sci.*, *45*, 3897–3910.
- Crook, N. A. (1996), Sensitivity of moist convection forced by boundary layer processes to low-level thermodynamic fields, *Mon. Weather Rev.*, *124*, 1767–1785.
- Dennis, E. J., and M. R. Kumjian (2017), The impact of vertical wind shear on hail growth in simulated supercells, *J. Atmos. Sci.*, *74*, 641–663.
- Fabry, F. (2006), The spatial variability of moisture in the boundary layer and its effect on convection initiation: Project-long characterization, *Mon. Weather Rev.*, *134*, 79–91.
- Foote, G. B. (1984), A study of hail growth utilizing observed storm conditions, *J. Clim. Appl. Meteorol.*, *23*, 84–101.
- Gilmore, M. S., J. M. Straka, and E. N. Rasmussen (2004), Precipitation and evolution sensitivity in simulated deep convective storms: Comparisons between liquid-only and simple ice and liquid phase microphysics, *Mon. Weather Rev.*, *132*, 1897–1916.
- Grant, L. D., and S. C. van den Heever (2014), Microphysical and dynamical characteristics of low-precipitation and classic supercells, *J. Atmos. Sci.*, *71*, 2604–2624.
- Guo, X., and M. Huang (2002), Hail formation and growth in a 3D cloud model with hail-bin microphysics, *Atmos. Res.*, *63*, 59–99.
- Heymsfield, A. J. (1982), A comparative study of the rates of development of potential graupel and hail embryos in High Plains storms, *J. Atmos. Sci.*, *39*, 2867–2897.
- Heymsfield, A. J., A. R. Jameson, and H. W. Frank (1980), Hail growth mechanisms in a Colorado storm: Part II: Hail formation processes, *J. Atmos. Sci.*, *37*, 1779–1807.
- Holloway, C. E., and J. D. Neelin (2009), Moisture vertical structure, column water vapor, and tropical deep convection, *J. Atmos. Sci.*, *66*, 1665–1683.
- Hong, S. Y., Y. Noh, and J. Dudhia (2006), A new vertical diffusion package with an explicit treatment of entrainment processes, *Mon. Weather Rev.*, *134*, 2318–2341.
- Johnson, D. E., P. K. Wang, and J. M. Straka (1993), Numerical simulations of the 2 August 1981 CCOPE supercell storm with and without ice microphysics, *J. Appl. Meteorol.*, *32*, 745–759.
- Johnson, D. E., P. K. Wang, and J. M. Straka (1994), A study of microphysical processes in the 2 August 1981 CCOPE supercell storm, *Atmos. Res.*, *33*, 93–123.
- Kennedy, P. C., and A. G. Detwiler (2003), A case study of the origin of hail in a multicell thunderstorm using in situ aircraft and polarimetric radar data, *J. Appl. Meteorol.*, *42*, 1679–1690.
- Li, M., Q. Zhang, and F. Zhang (2016), Hail day frequency trends and associated atmospheric circulation patterns over China during 1960–2012, *J. Clim.*, *29*, 7027–7044.
- Milbrandt, J. A., and M. K. Yau (2005a), A multimoment bulk microphysics parameterization. Part I: Analysis of the role of the spectral shape parameter, *J. Atmos. Sci.*, *62*, 3051–3064.
- Milbrandt, J. A., and M. K. Yau (2005b), A multimoment bulk microphysics parameterization. Part II: A proposed three-moment closure and scheme description, *J. Atmos. Sci.*, *62*, 3065–3081.
- Miller, L. J., J. D. Tuttle, and C. A. Knight (1988), Airflow and hail growth in a severe northern High Plains supercell, *J. Atmos. Sci.*, *45*, 736–762.
- Morrison, H., and J. A. Milbrandt (2011), Comparison of two-moment bulk microphysics schemes in idealized supercell thunderstorm simulations, *Mon. Weather Rev.*, *139*, 1103–1130, doi:10.1175/2010MWR3433.1.
- Morrison, H., J. A. Milbrandt, G. H. Bryan, K. Ikeda, S. A. Tessendorf, and G. Thompson (2015), Parameterization of cloud microphysics based on the prediction of bulk ice particle properties. Part II: Case study comparisons with observations and other schemes, *J. Atmos. Sci.*, *72*, 312–339.
- Nelson, S. P. (1983), The influence of storm flow structure on hail growth, *J. Atmos. Sci.*, *40*, 1965–1983.
- Rasmussen, R. M., and A. J. Heymsfield (1987), Melting and shedding of graupel and hail. Part II: Sensitivity study, *J. Atmos. Sci.*, *44*, 2764–2782.
- Richardson, Y. P., K. K. Droegemeier, and R. P. Davies-Jones (2007), The influence of horizontal environmental variability on numerically simulated convective storms. Part I: Variations in vertical shear, *Mon. Weather Rev.*, *135*, 3429–3455.
- Schlesinger, R. E. (1973), A numerical model of deep moist convection: Part I. Comparative experiments for variable ambient moisture and wind shear, *J. Atmos. Sci.*, *30*, 835–856.
- Schumacher, R. S. (2015), Sensitivity of precipitation accumulation in elevated convective systems to small changes in low-level moisture, *J. Atmos. Sci.*, *72*, 2507–2524.
- Skamarock, W. C., et al. (2008), A description of the advanced research WRF version 3, NCAR Tech. Note, NCAR/TN-4751STR, NCAR/MMM, 113 pp.
- Tao, W. K., and J. Simpson (1989), Modeling study of a tropical squall-type convective line, *J. Atmos. Sci.*, *46*, 177–202.
- Tao, W. K., J. Simpson, and S. T. Soong (1991), Numerical simulation of a subtropical squall line over the Taiwan Strait, *Mon. Weather Rev.*, *119*, 2699–2723.
- Tao, W. K., J. R. Scala, B. Ferrier, and J. Simpson (1995), The effect of melting processes on the development of a tropical and a midlatitude squall line, *J. Atmos. Sci.*, *52*, 1934–1948.
- van den Heever, S. C., and W. R. Cotton (2004), The impact of hail size on simulated supercell storms, *J. Atmos. Sci.*, *61*, 1596–1609.
- Weckwerth, T. M., et al. (2004), An overview of the International H₂O Project (IHOP_2002) and some preliminary highlights, *Bull. Am. Meteorol. Soc.*, *85*, 253–277.
- Yang, M. H., and R. A. Houze (1995), Sensitivity of squall-line rear inflow to ice microphysics and environmental humidity, *Mon. Weather Rev.*, *123*, 3175–3193.
- Ziegler, C. L., P. S. Ray, and N. C. Knight (1983), Hail growth in an Oklahoma multicell storm, *J. Atmos. Sci.*, *40*, 1768–1791.